Published in final edited form as:
J Neural Eng. 2014 October ; 11(5): 056014. doi:10.1088/1741-2560/11/5/056014.

Mechanically-Compliant Intracortical Implants Reduce the Neuroinflammatory Response

Jessica K. Nguyen[1,2], **Daniel J. Park**[1], **John L. Skousen**[2], **Allison E. Hess-Dunning**[2], **Dustin J. Tyler**[1,2], **Stuart J. Rowan**[1,3], **Christoph Weder**[3,4], and **Jeffrey R. Capadona**[1,2,*]

[1]Department of Biomedical Engineering, Case Western Reserve University, 2071 Martin Luther King Jr. Drive, Wickenden Bldg, Cleveland, OH 44106, USA [2]Advanced Platform Technology Center, Louis Stokes Cleveland Department of Veterans Affairs Medical Center, 10701 East Blvd, 151 W/APT, Cleveland, OH 44106-1702, USA [3]Department of Macromolecular Science and Engineering, Case Western Reserve University, 2100 Adelbert Road, Kent Hale Smith Bldg, Cleveland, OH 44106-7202, USA [4]Adolphe Merkle Institute, University of Fribourg, Route de l'Ancienne Papeterie, 1723 Marly, Switzerland

Abstract

Objective—The mechanisms underlying intracortical microelectrode encapsulation and failure are not well understood. A leading hypothesis implicates the role of the mechanical mismatch between rigid implant materials and the much softer brain tissue. Previous work has established the benefits of compliant materials on reducing early neuroinflammatory events. However, recent studies established late onset of a disease-like neurodegenerative state.

Approach—In this study, we implanted mechanically-adaptive materials, which are initially rigid but become compliant after implantation, to investigate the long-term chronic neuroinflammatory response to compliant intracortical microelectrodes.

Main results—Three days after implantation, during the acute healing phase of the response, the tissue response to the compliant implants was statistically similar to that of chemically matched stiff implants with much higher rigidity. However, at two, eight, and sixteen weeks post-implantation in the rat cortex, the compliant implants demonstrated a significantly reduced neuroinflammatory response when compared to stiff reference materials. Chronically implanted compliant materials also exhibited a more stable blood-brain barrier than the stiff reference materials.

Significance—Overall, the data show strikingly that mechanically-compliant intracortical implants can reduce the neuroinflammatory response in comparison to stiffer systems.

Keywords

Biomimetic material; Intracortical microelectrode; Foreign body response; Mechanical properties; Nanocomposite

[*]Denotes corresponding author: Direct correspondence to: Jeffrey R. Capadona, Ph.D., Case Western Reserve University, 2071 Martin Luther King Jr. Drive, Cleveland, OH, jeffrey.capadona@case.edu, Office: (216) 368-5486, Fax: (216) 368-1509.

The authors have no conflicts of interest related to this work to disclose.

1. Introduction

Intracortical microelectrodes that provide an electrical interface to the brain are potentially useful to achieve command, control, and feedback in numerous clinical applications. However, the clinical use of such devices is limited due to their inability to consistently record neural signals for extended periods (1). One of the main reasons for device failure is the body's natural inflammatory response directed against the implanted foreign object. In order to prevent inflammation and subsequent implant failure, engineers have designed devices with new architectures, bioactive coatings, or from alternative materials (2). Each of these approaches has demonstrated a clear short-term improvement in the neuroinflammatory response to implanted intracortical microelectrodes.

However, a disconnect remains between the time course in the neuroinflammatory response and failure in the ability to record neuronal action potentials (1, 3, 4). Two primary hypotheses have been presented to explain this temporal disconnect. The first is that recording inconsistencies are due to mechanical failure of the devices themselves (1, 5). However, a number of mechanical failure modes can be attributed to the reactive inflammatory environment, including oxidation and corrosion of the device (6, 7). Additionally, a majority of the studies examining the neuroinflammatory response to intracortical microelectrodes have been limited to timeframes of at most eight to twelve weeks post-implantation.

In an attempt to find a direct correlation between neural inflammation and device failure, several groups have begun exploring longer time points (for example, 16 weeks). Longer studies have resulted in the second leading hypothesis – the development of a late-onset, secondary neurodegenerative, disease-like state at the neural tissue-device interface (8). Specifically, some of us have observed that neuronal populations around traditional, rigid silicon implants were greatly reduced early after implantation, show a mid-term recovery, which is however followed by another decline (8). To date, it is unclear if, or when, the response stabilizes.

In previous studies, we have demonstrated that the mechanical mismatch between current neural devices and neural tissue is a significant contributor to the neuroinflammatory response (9, 10). We employed a new family of mechanically-adaptive nanocomposites, which change their mechanical properties from a rigid to a compliant state in less than 5 minutes after implantation (11, 12). The mechanically-adaptive nanocomposites were designed to support functional microelectrode components and enable implantation of highly compliant microelectrodes (13). For the application at hand, we developed materials that are initially stiff (tensile storage modulus E' ~5 GPa) to enable insertion into the brain tissue and then soften after implantation upon exposure to physiological conditions (E'~12 MPa) to more closely match the mechanical characteristics of the brain tissue (11, 14). Initial histological evaluations of these materials demonstrated that at four weeks post-implantation, compliant implants more rapidly stabilize neural cell populations at the device interface than rigid, non-dynamic microwire implants (9). However, in the light of our recent findings that the neuroinflammatory response to intracortical microelectrodes

fluctuates with time, we considered it important to extend our understanding of the neuroinflammatory response to compliant intracortical microelectrodes, particularly looking at time points corresponding to both early and late-onset neurodegeneration. Thus, we report herein on the acute and chronic inflammatory response of mechanically-adaptive neural interfaces and show significant differences to traditional rigid materials.

2. Materials and Methods

2.1 Intracortical Implants

For *in vivo* experiments, two different implants were used: (1) stiff poly(vinyl acetate)-coated silicon implants; and (2) mechanically-adaptive poly(vinyl acetate) / tunicate cellulose nanocrystal (tCNC) nanocomposites (NC), which become compliant after implantation. Single shank "Michigan" type silicon probes were fabricated in-house to a thickness of 15 μm, a length of 2 mm, and a shank width of 123 μm. PVAc-coated silicon implants (1) were created by dipcoating such silicon implants in a solution of PVAc in hot toluene (10% w/w at 70°C). Implants were dipped in succession twice, allowed to dry for 30 minutes to deposit a PVAc surface layer with a thickness of ~15 +/− 5 μm (Fig. 1). The thickness of the PVAc surface layer was determined using stylus profilometry (KLA-Tencor P-2 Long Scan Profilometer) at a scan rate of 50 μm/sec and stylus force of 12 mN. NC implants (2) were created by casting films from a solution of poly(vinyl acetate) (PVAc) and tCNC in dimethylformamide, as previously reported (11, 14). The NC had a tCNC content of 15% w/w. The resulting films were custom molded between sheets in a hot press (Carver, Wabash, IN). NC implants were then fabricated by laser-micromachining with a direct-write CO_2 laser (VLS 3.5, VersaLaser) to a thickness of ~63 μm, a length of 2 mm, and a shank width of 130–140 μm (13). All implants were ethylene oxide sterilized with the exception of sixteen week implants, which were UV sterilized before implantation. Previous work has established that sterilization method does not affect the inflammatory response at chronic time points (15).

2.2 Strain Field Modeling

To further understand the impact of varying implant stiffness and structural compliance on the surrounding brain tissue we developed a 3D finite-element model to simulate interfacial strains induced by brain micromotion as described previously (16, 17). All models were developed using COMSOL Multiphysics (COMSOL, Inc. Burlington, MA). In brief, the developed models consisted of two components: a single probe shank (modeled after each of the implants described above) and a surrounding brain tissue block. Taking advantage of symmetries in the model architecture only one quarter of the implanted region was modeled to facilitate visualization of the induced primary strains in the surrounding tissue. Brain tissue was approximated as linearly elastic with isotropic material properties as described by Taylor and Miller (18). The impact of a tangential tethering force on an implant fixed to the skull was simulated by applying a 20 μm displacement to the upper surface of the probe's shank.

The tensile storage modulus of silicon is between 130 and 185 GPa, while the tensile storage modulus of the NC is 5.2 GPa pre-insertion, and 12.7 MPa after insertion (11, 14). The NC

swells ~70% by volume under physiological conditions. Neat PVAc exhibits a tensile storage modulus of ~1.8 GPa pre-insertion, and ~1–12 MPa after insertion, and swells ~ 3–5% by volume when exposed to physiological conditions (14). Therefore, based on the law of mixtures for thin film composites (19), the composite modulus for the PVAc-coated silicon implants is between 49 and 78 GPa, i.e., significantly higher than that of the mechanically-adaptive nanocomposite in the compliant (post-insertion) state.

2.3 Animal Surgery

Surgical procedures for device implantation closely followed an established protocol, with only minor changes (8, 20, 21). Briefly, twenty-six male Sprague Dawley rats (250 – 300 grams) (Charles River, Spencerville, OH) received implants and were euthanized after three days or two, eight, or sixteen weeks. Eight additional animals were used as age-matched sham controls and did not undergo implantation surgery. Prior to surgery, animals were anesthetized with ketamine (80 mg/kg) and xylazine (10 mg/kg) administered intraperitoneally (IP). Once anesthetized, the surgical area was shaved, and then the animal was mounted on a stereotaxic frame and maintained on isofluorane (0.5–2%). A single injection of local anesthetic, Marcaine (0.5%), was administered below the incision site subcutaneously (SQ), then the surgical area was scrubbed with betadine and 70% isopropanol for sterilization. Animal body temperature was maintained on a circulating water pad and vitals were monitored using a blood-oxygen and heart rate measurement system (PulseSense, Nonin Medical, Inc,).

For implantation, a one-inch incision was made at midline using a scalpel and the skull was exposed. The surrounding tissue was retracted and a 3 mm hole was created in the skull, manually, using a biopsy punch (P/N #536, PSS Select), approximately 3 mm lateral to midline and 4 mm caudal to bregma. Then the dura was reflected using a 45 degree dura pick. Animals received a PVAc-coated silicon implant in one hemisphere and a NC implant in the contralateral hemisphere (n=5–7 for each time point), randomizing which implants were on each side. Implants are assumed to be independent of each other, as glial scarring has been demonstrated to extend up to 600 μm from the microelectrode/cortical tissue interface, without affecting the contralateral hemisphere (22, 23). All implants were inserted approximately 2 mm deep into the cortical tissue by hand. Implants were implanted perpendicular to the surface of the brain, to minimize the footprint of tissue damage, while avoiding larger vasculature. Following implantation, implants were tethered to the skull using Kwik-sil (World Precision Instruments) and UV-cured dental acrylic (Fusio- liquid dentin, Pentron Clinical) over the surgical area and skull. The incision was then closed with 5-0 monofilament polypropylene suture (Henry Schein) and a triple antibiotic ointment was applied to the incision. Once the animal woke from anesthesia, meloxicam (5 mg/kg, SQ) and cefazolin (16 mg/kg, SQ) were administered for potential pain and to prevent infection. Surgical procedures and animal care practices were performed in accordance with the Louis Stokes Cleveland Department of Veterans Affairs and Case Western Reserve University Institutional Animal Care and Use Committees (IACUC).

2.4 Tissue Processing

At three days, and two, eight and sixteen weeks post-implantation, animals were anesthetized using a mixture of ketamine (80 mg/kg) and xylazine (10 mg/kg) given IP. Each animal was perfused transcardially with 1X Phosphate Buffer Saline (PBS, Invitrogen) until the exudate was clear and then fixed with 10% formalin (~300 mL, VWR). The brain was carefully removed, placed in fresh 10% formalin and stored at 4° C until sectioning. Prior to sectioning, the tissue was cryoprotected in a step-wise gradient of 10%–20%–30% sucrose (Sigma) in 1X PBS at 4° C, until equilibrium was reached at each step. After equilibration in 30% sucrose, implants were removed from the brain tissue with forceps, and the tissue was frozen at −80° C in optimal cutting temperature compound (Tissue-Tek), sliced axially in 20 μm sections at −25°C, and mounted on slides to be stored at −80° C until immunohistochemical labeling.

2.5 Immunohistochemistry

Prior to immunolabeling, the tissue was removed from −80° C and equilibrated to room temperature in a humidity chamber to prevent tissue-drying. Optimal cutting temperature compound was removed with three washes in 1X PBS and then re-hydrated in 1X PBS containing 0.1% Triton-X 100 (Sigma) (1X PBS-T) for 15 minutes. Tissue was blocked for one hour at room temperature in goat serum blocking buffer (4% v/v serum (Invitrogen), 0.3% v/v Triton-X 100, 0.1% w/v sodium azide (Sigma)). Then, the tissue was incubated in primary antibody diluted in goat serum blocking buffer overnight at 4°C. Primary antibodies used were: mouse anti-neuronal nuclei (NeuN) (1:250, Millipore) for neurons, mouse anti-glial fibrillary acidic protein (GFAP) (1:500, Invitrogen) for astrocytes, rabbit anti-Iba1 (1:250, Wako) for all microglia/macrophages, mouse anti-CD68 (ED1) (1:100, Chemicon) for activated microglia/macrophages, and rabbit anti-immunoglobulin G (IgG) (1:100, AbD Serotec) for blood brain barrier permeability. After eighteen hours, the tissue was washed six times (5 minutes per wash) in 1X PBS-T, then stained for two hours at room temperature with appropriate Alexa Fluor conjugated secondary antibodies (diluted 1:1000 in blocking buffer) and counterstained with 4’,6-diamidino-2-phenylindole (DAPI) to mark total cell nuclei. The tissue was washed another six times (5 minutes per wash) in 1X PBS-T, then tissue autofluorescence was removed with a ten minute incubation in 0.5 mM copper sulfate buffer (50 mM Ammonium Acetate, pH 5.0) (Sigma) (20). Samples were rinsed with distilled water and mounted with Fluoromount-G (Southern Biotech).

Immunolabeled slides were imaged using a 10X objective on an AxioObserver Z1 (Zeiss, Inc.) and AxioCam MRm (Zeiss Inc.). For a larger field of view, without compromising resolution, mosaic images were obtained by stitching sixteen 10X images together using MosaiX software (Zeiss, Inc.). Exposure times were held constant for each respective cellular marker analyzed. Following acquisition, unaltered, linearized images were converted to 16-bit tagged imaging files (TIFs) using Axiovision LE (Zeiss Inc.) for minimal image compression to allow for optimal intensity analysis. For clarity in presentation only, images in this report have been pseudo-colored and slightly enhanced to improve visual display.

2.6 Quantitative Analysis

Following image acquisition, the images were converted to tagged imaging files (TIFs) for intensity analysis. All images except for NeuN were analyzed using MINUTE, a custom MATLAB program developed to analyze fluorescent intensity profiles around the implant (20). Briefly, the implant hole was manually defined for each image from the bright field image. Note, this method does not account for any small amount of tissue that may be removed with the explanted implant. The program then quantified the fluorescent intensity in 2 μm bins of expanding concentric circles around the implant hole up to 1500 μm away (0 μm is defined as the edge of the hole). Raw fluorescent intensities were normalized to background, defined as average intensity in the radii between 1000 to 1050 μm from the interface. Normalized fluorescent intensity profiles were obtained for each tissue section. After normalization, for statistical comparisons of each stain for the different implants, the area under the curve from 0 to 50, 50 to 100, 100 to 150, and 150 to 200 μm were obtained using MATLAB.

To quantify neuron populations around the implant site, the implant hole was manually defined and then expanding concentric circles up to 600 μm from the interface were defined for each NeuN image in Adobe Photoshop. The number of neurons in each ring was manually counted to obtain the number of neurons per area for each radial distance. Neuron counts were converted to percent to sham background by normalizing to neuron counts from age-matched sham animals at each respective time point.

2.7 Statistical Analysis

For statistical analysis, the area under the curve for all stains (except for NeuN) was used. For NeuN, the number of neurons per area was used for analysis. Statistical analyses were run using a general linear ANOVA model in Minitab 16 (Minitab Inc.) to allow for comparisons between the different implants. For significance, Tukey post-hoc tests were run for pairwise comparison and significance defined as $p<0.05$. For each animal, 6 images across the entire length of the implant were analyzed per stain; two from the top of the implant, two from the middle of the implant, and two from the tip of the implant. Therefore, with 5–7 animals per time point, 30–42 slices were imaged per stain. All images were then treated as an independent measurement and averaged with the entire group of images from a single cohort.

3. Results

In a comparative study, two implant types that serve as models for intracortical microelectrodes were implanted into the cortex of age-matched male rats. In order to investigate the role of material stiffness on tissue compliance-induced neuroinflammation, two types of implants were employed: 1) a polymer-coated silicon implant (PVAc-coated), designed to have a bulk stiffness close to the silicon implant and a surface chemistry that is matched to the nanocomposite; and 2) a compliant mechanically-adaptive polymer nanocomposite. Since the two implants are chemically matched, we will focus our nomenclature on the defining properties of each implant. Therefore, PVAc-coated implants will be referred to as “stiff” and NC implants will be referred to as “compliant.” It is

important to note that stress on surrounding tissue can be affected by various implant design parameters to reduce material compliance, such as modulus, size, or porosity. Therefore, here, we consciously utilize the term “compliant” instead of “soft” implant.

3.1 Finite Element Analysis of Tissue Strain

To better understand the influence of the varying stiffness within our two types of implants, we used a 3D finite element model to predict micromotion-induced strains surrounding our objects. The impact of a tangential tethering force on an implant fixed to the skull was simulated by applying a 20 μm displacement to the upper surface of the probes shank. The predictions made on this basis are shown in Fig. 2. Simulated micromotion surrounding tethered silicon devices with and without PVAc coating resulted in elevated strains both at the tip and at the sharp edges of the probe track in the tissue. The comparison predicts that nearly identical strain fields are exerted on the cortical tissue for both the bare silicon and silicon implants with a thin PVAc coating. Unlike previous models that examined a smaller total deflection (16), our model predicts that the greatest induced strain would be near the surface of the cortex rather than at the implants tip. When simulating the nanocomposite implant in the stiff state, it behaves similarly to the bare silicon and PVAc-coated silicon implants. By contrast, the model predicts that the nanocomposite implant in the compliant soft state behaves more like a (hypothetical) implant whose modulus matches that of the brain and induces considerably less strain on the surrounding tissue throughout all depths of the cortex.

3.2 Neuronal Nuclei

Theoretical modeling has suggested that neuronal cell bodies must be within the first 50 to 140 μm of the intracortical microelectrode in order to maintain recordings of action potentials from individual neurons (24). To quantify the number of neurons around the implants, we utilized the NeuN antibody, which selectively stains for neuronal nuclei (25). Representative fluorescence microscopy images of NeuN stained tissue can be found in Fig. 3. Each image corresponds to either the stiff (Fig. 3A,C,E,G) or the compliant (Fig. 3B,D,F,H) implant. The number of neurons per area was determined at regular intervals up to 600 μm from the material/tissue interface. The percent to sham was reported after normalizing the neuron counts to those of age-matched sham animals. At three days post-implantation, both implants exhibited significant neuronal loss compared to age-matched sham animals, up to 300 μm and 600 μm away from the implant for stiff and compliant implants, respectively. Further, there were no significant differences seen between the stiff and compliant implants (Fig. 3A–B,I). By two weeks, loss of neurons was indicated up to 200 μm from stiff implants compared to sham animals. However, neuronal densities were indistinguishable from sham tissue within only 50 μm from the surface of the compliant implant. Comparing the two implants, significant improvements in neuronal populations surrounding the compliant implant were seen between 50 and 200 μm from the implant surfaces (Fig. 3C–D,J). However, the neuron densities around the compliant implants remained comparable to the two week time point at eight weeks post-implantation. Significant difference between implant types at two weeks shifted to tissue volumes further from the implant surface (from 100–300 μm from implant surface at eight weeks post-implantation, Fig. 3E–F,K). Compared to age-matched sham animals, the stiff implants

demonstrated significant neuron loss up to 200 μm from the implant-tissue interface, while the compliant implants fully recovered to native levels by 100 μm. Most importantly, by sixteen weeks post-implantation, no neuronal loss was detected for the tissue surrounding the compliant implant, regardless of the distance from the implant. However, the stiff implants revealed appreciable neuronal loss in the most critical area within 50 μm from the implant surface, compared to both sham tissue and tissue surrounding compliant implants (Fig. 3G–H, L).

3.3 Glial Cell Markers

3.3.1 Astrocytes—Immunolabelling for GFAP was used to monitor both immature and mature resting or activated astrocytes (26). At three days post-implantation no appreciable glial scarring can be discerned (Fig. 4A–B,I), regardless of the type of implant. However, at all subsequent time points, immunostaining for GFAP showed a dense astrocytic scar around both the stiff and compliant implants (Fig. 4C–H, J–L). At two and eight weeks post-implantation, elevated levels of GFAP+ scarring around the stiff implant extended to a distance of ~500 μm away from the implant before the background levels were reached (Fig. 4C–F,J-K). By contrast, scarring around the compliant implant was contained to an area within a radius of 50 μm surrounding the implant. Significantly less GFAP expression was detected beyond 50 μm from the implant surface for compliant implants, compared to chemically matched stiff implants (Fig. 4C–F,J-K). By sixteen weeks, GFAP expression decreased for both implants (Fig. 4G–H,L). However, the normalized fluorescence intensity around the compliant implant still remained significantly lower than around the stiff implant in the area 0–100 μm away from the implantation site.

3.3.2 Microglia/Macrophages—Microglia/macrophages are a major component of the innate immune response in the CNS. Microglia/macrophage-released inflammatory factors sustain the innate immune/inflammatory response and recruit additional cell types. Therefore, we also investigated the spatial expression of all microglia and macrophages at the implant/tissue interface. The ionized calcium binding adapter molecule (Iba1) is a cell-surface marker for both resting and activated microglia/macrophages (27).

At three days post-implantation, increased Iba1+ immunoreactivity was observed out to a distance of 1 mm away from the implantation site (Fig. 5A–B,I). This could be due to either increased cell number or cellular activation causing up-regulation of Iba1 (27). The microglia/macrophages condensed around the implants by two weeks post-implantation (Fig. 5C–D,J). For both 3 days and 2 weeks post-implantation, no significant differences were seen between the stiff and compliant implants. However, eight weeks post implantation, the accumulation of microglia/macrophages around the compliant implants has become significantly more compact, as noted by a significant decrease in Iba1+ staining in the area between 50 to 150 μm away from the implant (Fig. 5E–F,K). Sixteen weeks post-implantation, an intense, circular zone of upregulated Iba1 immunoreactivity was observed around the stiff implant, whereas implant-mediated up-regulation of IBA1+ cells subsided to native levels and very little accumulation of microglia and macrophages were present around the compliant implant (Fig. 5G–H). Normalized average intensity profiles depict a higher peak intensity and broader distribution of Iba1+ immunoreactivity for the stiff

implants compared to the minimally up-regulated expression surrounding the mechanically compliant implant (Fig. 5L). Notably, after sixteen weeks, quantification of the Iba1 expression levels for the two conditions were significantly different over a distance of 75 μm from the implant, where a much larger distribution was seen in stiff implants than for compliant implants.

While Iba1 labels both resting and activated microglia/macrophages, CD68 is more regularly used to identify activated microglia/macrophages. CD68 is a cytoplasmic antigen found in the lysosomal compartment of activated microglia and macrophages (28). As seen with the Iba1 staining, at three days post-implantation there was activation of microglia/macrophages around both implants up to a distance of 1 mm away from the implantation site with no significant difference between implant types (Fig. 6A–B, I). However, after two weeks, the distribution of CD68+ immunoreactivity was more compact for both implants. Furthermore, there was a significant decrease in CD68+ staining surrounding the compliant implants in the area 0–100 μm away from the implant (Fig. 6C–D,J). At eight weeks post-implantation, there was a large drop in CD68+ staining surrounding both implants (Fig. 6E–F,K). However, there was significantly less CD68+ staining surrounding the compliant implant in the range 50–200 μm from the implantation site, suggesting a broader CD68+ cell distribution around the stiff implants. Representative images of CD68+ staining after sixteen weeks show very little microglia/macrophage activation at either interface (Fig. 6G–H). However, normalized intensity profiles do exhibit significantly more CD68 immunostaining at distances 0 to 50 μm away from the implant for the stiff material compared to the compliant implant (Fig. 6L). Further, the mechanically compliant implant lacked any appreciable presence of activated microglia or macrophages at the implant/tissue interface. Contrary, the stiff implant was accompanied by persistently activated microglia and macrophages at sixteen weeks post-implantation.

3.4 Blood Brain Barrier Integrity (IgG)

Insertion of the implant into the cortex causes blood brain barrier (BBB) damage and leakage of blood-derived cells and serum proteins into the cortical tissue. Additionally, inflammatory events, resulting from neurological disease or device implantation, can cause the BBB to remain open (29). The integrity of the BBB can be correlated to the amount of IgG present within the surrounding tissue (30, 31). Note that sodium fluorescein or Evans Blue albumin staining were not considered for this study as alternatives to IgG staining. While both have been shown to be valuable markers for blood-brain barrier permeability (32), either method limits the utility of the tissue for further histological evaluation, and typically requires additional dedicated animals. Therefore, to investigate BBB integrity, the amount of IgG present at the implant site was examined. Three days post implantation, the IgG accumulation around both implants is comparable, extending up to 1 mm away from the implantation site (Fig. 7A–B,I). After two weeks, there is a large increase in IgG present around the implant for both compliant and stiff implant types. However, there is significantly more accumulation of IgG around the stiff implant in the range of 100–500 μm away from the implantation site (Fig. 7C–D,J), compared to the compliant implant. After eight weeks, the integrity of the BBB is partially reestablished. IgG infiltration is reduced for both implants with the stiff implants still maintaining higher IgG levels in the range 100–

500 μm away from the implantation site (Fig. 7E–F,K). Representative fluorescence microscopy images of stained tissue showing IgG infiltration sixteen weeks post implantation reveal that the stiff implants prevented the complete healing of the BBB, as indicated by the diffuse, intense IgG staining of the tissue surrounding the implant surface (Fig. 7G). On the other hand, the mechanically compliant implants show significantly less deterioration of the BBB integrity (reduced IgG detection) around the implant site sixteen weeks post-implantation (Fig. 7H). Further, the stiff implants had a much higher peak intensity and broader infiltration of IgG into the brain tissue (300 μm) in comparison to the much softer compliant implant ($p<0.001$) (Fig. 7L).

Discussion

The base materials used for traditional microelectrodes are significantly stiffer and less compliant than cortical tissue (Fig. 2). Starting with Goldstein and Salcman's work in 1973, several groups have suggested that motion of the brain with respect to the microelectrode may induce damage to the surrounding tissue (9, 10, 16, 33–36). Recently, Moshayedi *et al*. reported that astrocytes and microglia respond to surface stiffness and under acute conditions show enhanced foreign body response to stiff implants (37). Therefore, this study was designed to investigate the temporal effects of the stiffness of the microelectrode implant on the neurodegenerative inflammatory response. In order to keep the study as simple as possible, experiments were not conducted with functional microelectrodes, but with simple shanks made from base materials with different properties.

Utilizing the same nanocomposite materials as we present here, we previously demonstrated in an initial study that at four weeks post-implantation, neuronal densities were higher surrounding compliant implants than stiff microwires (9). However, the beneficial effects of material modulus appeared to depreciate by eight weeks post-implantation. While these results may indicate that mechanical mismatch has limited effects on the chronic inflammatory response, the Tresco lab has observed that microwire implants produce a reduced inflammatory response compared to Michigan-style implants (38). Previous work also has indicated that mechanics and architecture can each independently manipulate the inflammatory response (31, 39–41). Additionally, we have previously reported that rigid silicon implants show a mid-term recovery phase in neuron densities (8). Therefore, the lack of difference at eight weeks may be due to differences in implant architecture, or a recovery phase.

To verify this interpretation, we here undertook a comprehensive evaluation of the neuroinflammatory response to nanocomposite implants using Michigan-style controls. In order to investigate the role that implant compliance has on the neuroinflammatory response, implants fabricated from a previously reported mechanically adaptive material, which becomes compliant upon exposure to physiological conditions, were implanted into the cortex of rats for three days, two weeks, eight weeks or sixteen weeks. PVAc-coated silicon microelectrodes were implanted in the contralateral hemisphere to serve as a stiff control with a chemically-matched surface. Findings from this study demonstrate that mechanically compliant intracortical implants elicit a reduced neuroinflammatory response, resulting in significantly less neurodegeneration and a more robust BBB than chemically matched stiff

implants at two, eight, and sixteen weeks, but not 3 days post-implantation. Interestingly, in contrast to our previous initial study, few statistically significant differences were observed between compliant and stiff PVAc implants at early time points. Additionally, various differences in glial scar immunoreactivity between this study and the initial study were observed at eight weeks post-implantation. These discrepancies could be due to differences in the controls, surgical procedures, analysis methods, or other factors. Several groups have been working to overcome such potential inconsistencies by creating standardized techniques. Unfortunately, a consensus on methodology has not been reached by the field. Therefore, the discussion here will focus on placing the current results into context. The authors also note that the compliant implants had larger dimensions than the stiff controls due to fabrication limitations of the polymer nanocomposite materials. However, despite this difference in size, the compliant implants still significantly reduced neuroinflammatory events.

A leading hypothesis for the loss of electrical contact with implanted microelectrodes is the decrease in viability of neuron populations around the implant. Therefore, we first investigated the neuron density around each implant to determine if there was a benefit to using a softer, more compliant implant on neuronal survival. Glial scarring has been demonstrated to extend beyond 600 μm from the microelectrode/cortical tissue interface (22). However, neuronal ‘die back’ is typically understood to extend only a few hundred micrometers or less away from the implant (42–44). Compared to age-matched sham animals, stiff implants exhibit significant reduction in neuron densities at all of the time points investigated (Fig. 3, #$p<0.05$). The loss of neurons surrounding the implant may indicate neurodegeneration or mechanical movement of the cells. At three days post-implantation, both the compliant and stiff fail to demonstrate statistically different neuronal populations when compared to each other. However, neuronal dieback extends out 300 μm further (to 600 μm) for the stiff implants than for the compliant implants. The increased tissue volume in which significant neurons densities are lost for stiff implants suggests that the compliance of the implant plays a role in neuronal loss, even during the acute phases of wound healing. However, our results further suggest that at such acute time points, the mechanics of the implant may not be able to completely abolish neuronal loss around the devices.

Starting at 2 weeks post-implantation, the compliant implants exhibited increased neuronal populations compared to their stiff counterparts. While at two and eights week neuronal populations gradually increased surrounding both implants, the number of neurons around the compliant implants improved significantly compared to the stiff implants, starting at two weeks. Additionally, after sixteen weeks, examination of neuron populations surrounding the two probes indicated a significant advantage of the mechanically compliant implant within the first 50 μm from the implant. Only the compliant implant supported full recovery of neuronal populations near the implant surface, which is critical to obtain single unit recordings (24).

Next, we investigated the primary markers of the glial scar, known to rapidly encapsulate implanted microelectrodes (1–3, 45). Astrocytes form a major component of the glial scar around the electrode. This cellular encapsulation can result in increased impedance around

the electrode, making recordings more difficult to maintain (46). However, some glial scar formation is desirable to stabilize and anchor the electrode in the brain (17). Additionally, microglia/macrophages mediate the inflammatory and immune response to minimize bacterial/viral invaders (47), as well as infiltrating blood proteins within the CNS (48). Therefore, many studies of the tissue response to intracortical electrodes have focused on microglia/macrophage activation in response to indwelling implants (2).

Like NeuN staining, the quantified intensity of GFAP, Iba1, and CD68 stained tissue around the implant was the same for both implants at three days post-implantation (Fig. 4–6, A,B,I). Similarities in the acute inflammatory responses to both implants suggest that wound healing events may dominate the tissue reaction at this early time point. Much is known about the role of early wound healing events in injury and other device implantation models (49, 50). However, when considering intracortical microelectrodes, comparably few studies have explored the early wound healing events after implantation (51). The majority of what is known about the brain's response to implanted microelectrodes comes from end-point histological studies focused on later time points that range from ~1–24 weeks post-implantation. However, Biran *et al*. compared various markers of neuroinflammation in chronically implanted animals to animals that received only a stab wound injury (52). The authors found that chronic neuroinflammation does not accompany stab wound injuries made with identical recording devices. Therefore, the lack of difference in the neurodegenerative and neuroinflammatory response at three days post-implantation is somewhat expected.

By two weeks, the GFAP+ staining surrounding compliant implants is significantly less dense than that displayed in the tissue surrounding stiff control implants. Increased astrocytic reactivity around stiff implants, which are predicted to have increased tissue strain, are consistent with findings from Biran *et al*. Biran controlled tissue strain through the comparison of a tethered versus untethered electrode and established the connection between increased tissue strain and increased tissue reactivity (42). Therefore, our results also suggest that decreased prevalence of an astrocyte-rich glial scar may be a consequence of the mechanically compliant implants producing less strain on the tissue. Similarly, at later time points, the glial scarring around the compliant implant has lower peak intensity and is more compact. Interestingly, there appears to be a spatial relationship between the ranges of increased neuronal populations and decreased glial scarring surrounding the compliant implants. Specifically, the glial scar peaks until about 100 μm away from the compliant at two and eight weeks post-implantation, which corresponds to regions where the compliant implant also preserves significantly higher neuronal densities. Together, the decreased glial scarring and increased neuronal populations surrounding compliant implants promises to prevent increased impedance often associated with more stiff implants, thus allowing for improved neural recordings from the increased population of remaining neurons.

Our assessment of microglia/macrophages around the compliant implant showed reduced Iba1 (all microglia/macrophages) (Fig. 5) and CD68 (activated microglia/macrophages) immunoreactivity (Fig. 6) compared to the stiff implants beginning two weeks post-implantation. While at two weeks there is no difference in total microglia/macrophages, there is a significant increase in the activation of microglia/macrophages (Fig. 6, C–D)

surrounding the stiff implant. This suggests that material modulus may affect the activation of microglia/macrophages but does not prevent accumulation of cells at the site of injury. After sixteen weeks, activated microglia/macrophage populations surrounding compliant implants were equivalent to background sham controls, regardless of the distance from the implant (Fig. 6 H, L). Interestingly, CD68 staining for activated microglia/macrophages was in excellent agreement with NeuN staining, suggesting a correlation between microglia activation and neuron viability as an effect of implant stiffness. Several studies have indicated a large number of activated microglia cells on the implant surface long after the initial wound healing response is complete. Activated microglia and macrophages release a plethora of pro-inflammatory/cytotoxic soluble factors that can damage healthy bystander cells and the surrounding tissue (53–57). Pro-inflammatory cytokines can have direct toxic effects on neurons and oligodendrocytes, while reactive oxygen species and chemokines are involved in opening the BBB and recruiting new macrophages to sites of injury and inflammation (58). Several recent studies have also provided further support for the predominant role of macrophage-released factors on the recording function and the neuroinflammatory response. For example, Karumbaiah *et al*. have shown that gene expression for various pro-inflammatory soluble factors is up-regulated in tissue surrounding poorly performing microelectrodes (59). In addition, Skousen *et al*. have suggested that macrophage-secreted soluble factors may be critical in both propagating as well as shaping the response to traditional microelectrode designs (31).

Gilletti and Muthuswamy have demonstrated that implants in the cortex of rats can move on the order of 10–30 μm due to pressure changes during respiration, and 2–4 μm due to vascular pulsatility (60). They concluded that such significant micromotion can impact a wide variety of acute and chronic procedures involving any brain implant. Since the brain is highly vascularized (61), continual pulsatile activity of implants may also lead to the repetitive trauma to micro-vessels. Vascular damage, combined with increased release of reactive oxygen species and chemokines, can cause a constant influx of blood-derived cells and neurotoxic serum proteins (58). Irregularities in the stability of the BBB functionality are increasingly investigated in implant-associated disease-like states, due to the neurodegenerative role of several plasma proteins.

Therefore, to visualize BBB permeability, we stained for IgG, a common blood derived protein not typically found in neural tissue (62). Interestingly, maximal IgG+ staining was not apparent until two weeks post-implantation. Saxena *et al*. also investigated a three day time point and saw minimal IgG staining (40), which was attributed to brain edema found to be maximal at three days post-trauma. Starting at two weeks post-implantation, both compliant and stiff implants exhibited a significant increase in accumulated IgG within the cortical tissue. However, the stiff implant facilitated a much broader distribution of IgG+ tissue. Notably, at sixteen weeks post-implantation, there were still considerable amounts of IgG present at the injury site for both compliant and stiff implants. Here, staining for IgG was in agreement with the same volume of tissue supporting increased levels of CD68+ cells and the lowest levels of NeuN+ cells. However, it remains unclear if the compliant material facilitates less initial damage to the BBB, or if the softer material has the same initial

damage but allows for a more complete repair due to reduction in micromotion induced damage.

As indicated previously, the compliant material swells considerably while becoming compliant, creating an additional factor to consider in this study. Skousen et al. investigated the utility of hydrogel coatings on microelectrodes and noted that they can create “cytokine sinks” (63). While absorption of pro-inflammatory molecules is possible, the porosity of our material most likely impedes the uptake of proteins during swelling, and was not investigated here. Additionally, aqueous uptake creates challenges for engineering functional microelectrodes for neural recordings. The Tyler and Zorman labs are currently developing microsystems with our mechanically dynamic materials, in which the compliant material serves as a substrate to replace rigid silicon. Their design utilizes insulating materials to isolate the water soaked compliant material from the electrodes (13).

From the above described experiments, we have demonstrated that the more compliant implants demonstrate a significant reduction in several markers of glial scarring, BBB stability, and an increased neuron density (Fig. 8) compared to the stiff, chemically matched control implants. To date, there have been limited efforts to directly measure the strain on cortical neural tissue following device implantation. While LaPlaca and colleagues have demonstrated *in vitro* that strain can cause reactive gliosis and neuron loss (64), experiments are difficult to reproduce *in vivo*. Interestingly, Bellamkonda and colleagues have reported that low magnitude strain on astrocytes and microglia induced up-regulation of IL-36Ra as early as three days post-implantation, which was correlated with increased neuronal apoptosis (59). In agreement with both LaPlaca and Bellamkonda’s work, the acute study by Moshayedi *et al*. reported that astrocytes and microglia both respond to surface stiffness, facilitating differences in the foreign body response (37). However, the effect seen by Bellamkonda was less pronounced by twelve weeks post-implantation, presumably due to strain shielding of cortical tissue by more robust glial scars. Supporting this hypothesis, Muthuswamy and coworkers (65) recently reported on changes in the mechanical properties in the brain-electrode interface during chronic implantation. Using a customized jig, a microelectrode was immobilized onto the skull and chronic force measurements obtained with a tension/compression load cell at various time points. *In vivo* measurements of strain and micromotion stresses surrounding microelectrode implants indicated changes in estimated elastic modulus of the surrounding brain tissue.

The data presented here suggest that the effects of mechanical mismatch between compliant neural tissue and the implanted microelectrode may play a role in neuroinflammation and indicate a dominant role of the mechanical stiffness of the implant during chronic conditions. It is critical that future studies exploit cutting edge methods developed by groups such as the Muthuswamy Lab, using novel materials, such as those used here, in order to better understand how device stiffness/compliance results in changes in the duration and magnitude of strain and micromotion stresses surrounding microelectrode implants.

5. Conclusions

The results presented in this study support the hypothesis that late-onset neuron loss may be attributed to continuous mechanical damage from the mechanical mismatch of stiff implants. While previous studies have indicated the advantage of compliant implants in reducing acute neuroinflammatory responses, here we gathered new insights on the long-term effects of compliant implants. Specifically, we found that while wound healing events dominated acute inflammatory events, tissue surrounding the compliant implants at later time points demonstrated a significant reduction in the expression of glial scar formation markers, and a significant increase in neuron density compared to stiffer implants. Of note, neuronal viability appeared to be related to low microglial activity and reduced BBB permeability. Further work is required to pinpoint the exact mechanism and causal relationship between mechanical, chemical, inflammatory events, and the role of BBB stability. However, we have demonstrated that at extended periods post-implantation, mechanically compliant materials present a significant advantage in stabilizing the neural interface. It will be critical to next explore how these changes in neuroinflammatory events directly relate to tissue strain and how functional neural electrodes derived from compliant substrates mediate the stability of neural recordings and/or the function of other neural implants that suffer from decreased device performance due to an encapsulating glial scar.

Acknowledgments

This work was supported by the Department of Biomedical Engineering at Case Western Reserve University through laboratory start-up funds (Capadona). The research described here was supported in part by each of the following: Department of Veterans Affairs, Veterans Health Administration, Rehabilitation Research and Development Service: Career Development Award (B6344W, Capadona), Merit Review (B7122R, Capadona), the Advanced Platform Technology Center (C3819C), and Presidential Early Career Award for Scientists and Engineers (PECASE, Capadona); the National Institutes of Health: National Institute of Biomedical Imaging and Bioengineering Integrated Engineering and Rehabilitation Training Program (5T32EB004314-15), National Institute of Neurological Disorders and Stroke (R01- NS082404-01A1, Capadona and R21-NS053798, Tyler); National Science Foundation: (CBET-0828155, DMR-0804874 and DMR-1204948, Weder and Rowan); the Swiss National Science Foundation (NRP 62: Smart Materials, Nr. 406240_126046, Weder); and the Adolphe Merkle Foundation (Weder). The authors also thank L. Hsu for providing the dynamic materials. None of the funding sources aided in the collection, analysis and interpretation of data, in the writing of the report, or in the decision to submit the paper for publication.

References

1. Ward MP, Rajdev P, Ellison C, Irazoqui PP. Toward a comparison of microelectrodes for acute and chronic recordings. Brain Res. 2009; 1282:183–200. [PubMed: 19486899]
2. Tresco PA, Winslow BD. The challenge of integrating devices into the central nervous system. Crit Rev Biomed Eng. 2011; 39(1):29–44. [PubMed: 21488813]
3. He, W.; Bellamkonda, RV. A molecular perspective on understanding and modulating the performance of chronic central nervous system (CNS) recording electrodes. In: Reichert, WM., editor. Indwelling Neural Implants: Strategies for Contending with the In Vivo Environment. Boca Raton (FL): CRC Press; 2008.
4. Prasad A, Xue Q-S, Sankar V, Nishida T, Shaw G, Streit WJ, et al. Comprehensive characterization and failure modes of tungsten microwire arrays in chronic neural implants. J Neural Eng. 2012; 9(5):056015. [PubMed: 23010756]
5. Barrese JC, Rao N, Paroo K, Triebwasser C, Vargas-Irwin C, Franquemont L, et al. Failure mode analysis of silicon-based intracortical microelectrode arrays in non-human primates. J Neural Eng. 2013; 10(6):066014. [PubMed: 24216311]

6. Sanchez JC, Alba N, Nishida T, Batich C, Carney PR. Structural modifications in chronic microwire electrodes for cortical neuroprosthetics: a case study. IEEE transactions on neural systems and rehabilitation engineering : a publication of the IEEE Engineering in Medicine and Biology Society. 2006; 14(2):217–221.
7. Patrick E, Orazem ME, Sanchez JC, Nishida T. Corrosion of tungsten microelectrodes used in neural recording applications. J Neurosci Methods. 2011; 198(2):158–171. [PubMed: 21470563]
8. Potter KA, Buck AC, Self WK, Capadona JR. Stab injury and device implantation within the brain results in inversely multiphasic neuroinflammatory and neurodegenerative responses. J Neural Eng. 2012; 9(4):046020. [PubMed: 22832283]
9. Harris JP, Capadona JR, Miller RH, Healy BC, Shanmuganathan K, Rowan SJ, et al. Mechanically adaptive intracortical implants improve the proximity of neuronal cell bodies. J Neural Eng. 2011; 8(6):066011. [PubMed: 22049097]
10. Harris JP, Hess AE, Rowan SJ, Weder C, Zorman CA, Tyler DJ, et al. In vivo deployment of mechanically adaptive nanocomposites for intracortical microelectrodes. J Neural Eng. 2011; 8(4): 046010. [PubMed: 21654037]
11. Capadona JR, Shanmuganathan K, Tyler DJ, Rowan SJ, Weder C. Stimuli-responsive polymer nanocomposites inspired by the sea cucumber dermis. Science. 2008; 319(5868):1370. [PubMed: 18323449]
12. Capadona JR, Tyler DJ, Zorman CA, Rowan SJ, Weder C. Mechanically adaptive nanocomposites for neural interfacing. MRS Bull. 2012; 37(06):581–589.
13. Hess A, Capadona J, Shanmuganathan K, Hsu L, Rowan S, Weder C, et al. Development of a stimuli-responsive polymer nanocomposite toward biologically-optimized, MEMS-based neural probes. J Micromech Microeng. 2011; 21:54009–54017.
14. Shanmuganathan K, Capadona JR, Rowan SJ, Weder C. Stimuli-responsive mechanically adaptive polymer nanocomposites. ACS Appl Mater Inter. 2010; 2(1):165–174.
15. Ravikumar, m; Hageman, DJ.; Tomaszewski, WH.; Chandra, GM.; Skousen, JL.; Capadona, JR. The effect of residual endotoxin contamination on the neuroinflammatory response to sterilized intracortical microelectrodes. J Mater Chem B. 2014; 2:2517–2529.
16. Subbaroyan J, Martin DC, Kipke DR. A finite-element model of the mechanical effects of implantable microelectrodes in the cerebral cortex. J Neural Eng. 2005; 2(4):103–113. [PubMed: 16317234]
17. Lee H, Bellamkonda RV, Sun W, Levenston ME. Biomechanical analysis of silicon microelectrode-induced strain in the brain. J Neural Eng. 2005; 2(4):81–89. [PubMed: 16317231]
18. Zhao L, Lee JY, Hwang DH. Inhibition of pattern recognition receptor-mediated inflammation by bioactive phytochemicals. Nutr Rev. 2011; 69(6):310–320. [PubMed: 21631512]
19. Parro RJ, Scardelletti MC, Varaljay NC, Zimmerman S, Zorman CA. Amorphous SiC as a structural layer in microbridge-based RF MEMS switches for use in software-defined radio. Solid-State Electronics. 2008; 52(10):1647–1651.
20. Potter KA, Simon JS, Velagapudi B, Capadona JR. Reduction of autofluorescence at the microelectrode-cortical tissue interface improves antibody detection. J Neurosci Methods. 2012; 203(1):96–105. [PubMed: 21978484]
21. Potter-Baker KA, Ravikumar M, Burke AA, Meador WD, Householder KT, Buck AC, et al. A comparison of neuroinflammation to implanted microelectrodes in rat and mouse models. Biomaterials. 2014; 34:5637–5646. [PubMed: 24755527]
22. Turner JN, Shain W, Szarowski DH, Andersen M, Martins S, Isaacson M, et al. Cerebral astrocyte response to micromachined silicon implants. Exp Neurol. 1999; 156(1):33–49. [PubMed: 10192775]
23. Lind G, Gällentoft L, Danielsen N, Schouenborg J, Pettersson LM. Multiple implants do not aggravate the tissue reaction in rat brain. PLoS One. 2012; 7(10):e47509. [PubMed: 23091629]
24. Buzsáki G. Large-scale recording of neuronal ensembles. Nat Neurosci. 2004; 7(5):446–451. [PubMed: 15114356]
25. Mullen RJ, Buck CR, Smith AM. NeuN, a neuronal specific nuclear protein in vertebrates. Development. 1992; 116:201–211. [PubMed: 1483388]

26. Eddleston M, Mucke L. Molecular profile of reactive astrocytes- implications for their role in neurologic disease. Neuroscience. 1993; 54(1):15–36. [PubMed: 8515840]
27. Ito D, Imai Y, Ohsawa K, Nakajima K, Fukuuchi Y, Kohsaka S. Microglia-specific localisation of a novel calcium binding protein, Iba1. Brain Res Mol Brain Res. 1998; 57:1–9. [PubMed: 9630473]
28. Dijkstra C, Dopp E, Joling P, Kraal G. The heterogeneity of mononuclear phagocytes in lymphoid organs: distinct macrophage subpopulations in the rat recognized by monoclonal antibodies ED1, ED2 and ED3. Immunology. 1985; 54:589–599. [PubMed: 3882559]
29. Vries, HEd; Blom-Roosemalen, MCM.; Oosten, Mv; Boer, AGd; Berkel, TJCv; Breimer, DD., et al. The influence of cytokines on the integrity of the blood-brain barrier in vitro. J Neuroimmunol. 1996; 64:37–43. [PubMed: 8598388]
30. McConnell GC, Rees HD, Levey AI, Gutekunst C-A, Gross RE, Bellamkonda RV. Implanted neural electrodes cause chronic, local inflammation that is correlated with local neurodegeneration. J Neural Eng. 2009; 6(5):056003. [PubMed: 19700815]
31. Skousen J, Merriam S, Srivannavit O, Perlin G, Wise K, Tresco P. Reducing surface area while maintaining implant penetrating profile lowers the brain foreign body response to chronically implanted planar silicon microelectrode arrays. Prog Brain Res. 2011; 194C:167–180. [PubMed: 21867802]
32. Hawkins BT, Egleton RD. Fluorescence imaging of blood–brain barrier disruption. J Neurosci Methods. 2005; 151(2):262–267. [PubMed: 16181683]
33. Goldstein SR, Salcman M. Mechanical factors in the design of chronic recording intracortical microelectrodes. IEEE Trans Biomed Eng. 1973; 20(4):260–269. [PubMed: 4196687]
34. Kim DH, Abidian M, Martin DC. Conducting polymers grown in hydrogel scaffolds coated on neural prosthetic devices. J Biomed Mater Res A. 2004; 71(4):577–585. [PubMed: 15514937]
35. Hess, A.; Dunning, J.; Harris, J.; Capadona, JR.; Shanmuganathan, K.; Rowan, SJ., et al. A bio-inspired, chemo-responsive polymer nanocomposite for mechanically dynamic microsystems; Denver. Solid-State Sensors, Actuators and Microsystems Conference, 2009 TRANSDUCERS 2009 International; 2009 Jun 21–25. p. 224-227.CO2009
36. Ware T, Simon D, Arreaga-Salas DE, Reeder J, Rennaker R, Keefer EW, et al. Fabrication of responsive, softening neural interfaces. Adv Funct Mater. 2012; 22(16):3470–3479.
37. Moshayedi P, Ng G, Kwok JCF, Yeo GSH, Bryant CE, Fawcett JW, et al. The relationship between glial cell mechanosensitivity and foreign body reactions in the central nervous system. Biomaterials. 2014; 35(13):3919–3925. [PubMed: 24529901]
38. Winslow BD, Tresco PA. Quantitative analysis of the tissue response to chronically implanted microwire electrodes in rat cortex. Biomaterials. 2009 Dec 4.
39. Winslow BD, Christensen MB, Yang WK, Solzbacher F, Tresco PA. A comparison of the tissue response to chronically implanted Parylene-C-coated and uncoated planar silicon microelectrode arrays in rat cortex. Biomaterials. 2010; 31(35):9163–9172. [PubMed: 20561678]
40. Saxena T, Karumbaiah L, Gaupp EA, Patkar R, Patil K, Betancur M, et al. The impact of chronic blood–brain barrier breach on intracortical electrode function. Biomaterials. 2013; 34(20):4703–4713. [PubMed: 23562053]
41. Karumbaiah L, Saxena T, Carlson D, Patil K, Patkar R, Gaupp EA, et al. Relationship between intracortical electrode design and chronic recording function. Biomaterials. 2013; 34(33):8061–8074. [PubMed: 23891081]
42. Biran R, Martin DC, Tresco PA. The brain tissue response to implanted silicon microelectrode arrays is increased when the device is tethered to the skull. J Biomed Mater Res A. 2007; 82(1): 169–178. [PubMed: 17266019]
43. McConnell, GC.; Schneider, TM.; Bellamkonda, RV., editors. Acute spatiotemporal changes in neuronal density surrounding microelectrode arrays implanted in rat motor cortex; Kohala Coast, HI. Neural Engineering, 2007 CNE '07 3rd International IEEE/EMBS Conference on; 2007 May 2–5. 2007
44. Woolley AJ, Desai HA, Otto KJ. Chronic intracortical microelectrode arrays induce non-uniform, depth-related tissue responses. J Neural Eng. 2013; 10(2):026007. [PubMed: 23428842]

45. Szarowski DH, Andersen MD, Retterer S, Spence AJ, Isaacson M, Craighead HG, et al. Brain responses to micro-machined silicon devices. Brain Res. 2003; 983(1–2):23–35. [PubMed: 12914963]
46. Williams JC, Hippensteel JA, Dilgen J, Shain W, Kipke DR. Complex impedance spectroscopy for monitoring tissue responses to inserted neural implants. J Neural Eng. 2007 Dec; 4(4):410–423. [PubMed: 18057508]
47. Kreutzberg GW. Microglia: a sensor for pathological events in the CNS. Trends Neurosci. 1996; 19(8):312–318. [PubMed: 8843599]
48. Arroyo DS, Soria JA, Gaviglio EA, Rodriguez-Galan MC, Iribarren P. Toll-like receptors are key players in neurodegeneration. Int Immunopharmacol. 2011; 11(10):1415–1421. [PubMed: 21616174]
49. Anderson JM. Biological responses to materials. Annu Rev Mater Res. 2001; 31:81–110.
50. Anderson JM, Rodriguez A, Chang DT. Foreign body reaction to biomaterials. Semin Immunol. 2008; 20:86–100. [PubMed: 18162407]
51. Pollock AL. Early Brain Tissue Reaction Surrounding the Michigan-style Microelectrode Arrays Indicates that Extensive Remodeling of Glial and Neuronal Populations Occurs During the Foreign Body Response: Department of Bioengineering, University of Utah. 2007
52. Biran R, Martin DC, Tresco PA. Neuronal cell loss accompanies the brain tissue response to chronically implanted silicon microelectrode arrays. Exp Neurol. 2005; 195(1):115–126. [PubMed: 16045910]
53. Chao CC, Hu S, Peterson PK. Glia, cytokines, and neurotoxicity. Crit Rev Neurobiol. 1995; 9(2–3):189–205. [PubMed: 8581983]
54. Hanisch UK, Kettenmann H. Microglia: active sensor and versatile effector cells in the normal and pathologic brain. Nat Neurosci. 2007; 10(11):1387–1394. [PubMed: 17965659]
55. Mantovani A, Sozzani S, Locati M, Allavena P, Sica A. Macrophage polarization: tumor-associated macrophages as a paradigm for polarized M2 mononuclear phagocytes. Trends Immunol. 2002; 23(11):549–555. [PubMed: 12401408]
56. Quagliarello VJ, Wispelwey B, Long WJ Jr, Scheld WM. Recombinant human interleukin-1 induces meningitis and blood-brain barrier injury in the rat. Characterization and comparison with tumor necrosis factor. J Clin Invest. 1991; 87(4):1360–1366. [PubMed: 2010549]
57. Block ML, Zecca L, Hong J-S. Microglia-mediated neurotoxicity: uncovering the molecular mechanisms. Nat Rev Neurosci. 2007; 8(1):57–69. [PubMed: 17180163]
58. Potter KA, Buck AC, Self WK, Callanan ME, Sunil S, Capadona JR. The effect of resveratrol on neurodegeneration and blood brain barrier stability surrounding intracortical microelectrodes. Biomaterials. 2013; 34:7001–7015. [PubMed: 23791503]
59. Karumbaiah L, Norman SE, Rajan NB, Anand S, Saxena T, Betancur M, et al. The upregulation of specific interleukin (IL) receptor antagonists and paradoxical enhancement of neuronal apoptosis due to electrode induced strain and brain micromotion. Biomaterials. 2012; 33(26):5983–5996. [PubMed: 22681976]
60. Gilletti A, Muthuswamy J. Brain micromotion around implants in the rodent somatosensory cortex. J Neural Eng. 2006; 3(3):189–195. [PubMed: 16921202]
61. Wong-Riley MTT. Cytochrome oxidase: an endogenous metabolic marker for neuronal activity. Trends Neurosci. 1989; 12(3):94–101. [PubMed: 2469224]
62. Aihara N, Tanno H, Hall JJ, Pitts LH, Noble LJ. Immunocytochemical localization of immunoglobulins in the rat brain: relationship to the blood-brain barrier. J Comp Neurol. 1994; 342:481–496. [PubMed: 8040362]
63. Skousen, JL. Novel design strategies to reduce the foreign body response to central nervous system implants [PhD]. Salt Lake City: University of Utah; 2013.
64. Cullen DK, Simon CM, LaPlaca MC. Strain rate-dependent induction of reactive astrogliosis and cell death in three-dimensional neuronal-astrocytic co-cultures. Brain Res. 2007; 1158:103–115. [PubMed: 17555726]
65. Sridharan A, Rajan S, Muthuswamy J. Long-term changes in the material properties of brain-tissue at the implant-tissue interface. J Neural Eng. 2013; 10(6):066001. [PubMed: 24099854]

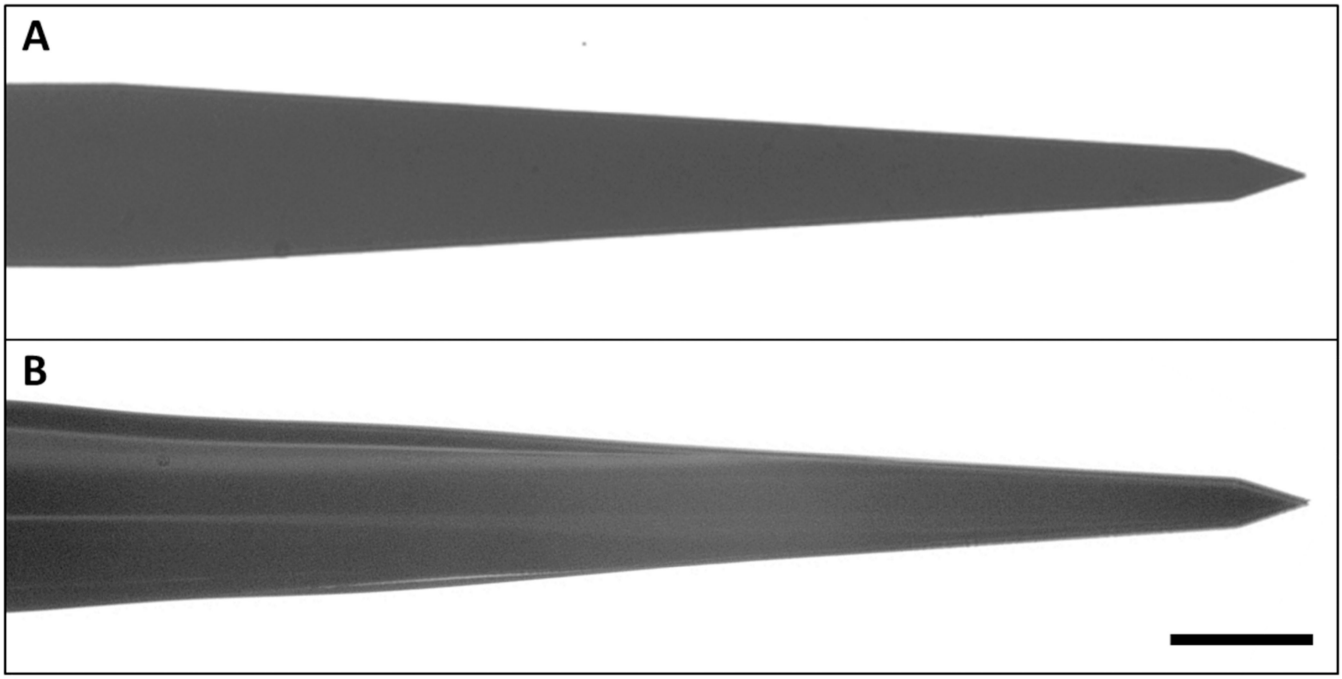

Figure 1.
Images of Michigan-style silicon probes before (A) and after (B) PVAc coating. Dipcoating deposited a PVAc-surface layer of 15 ± 5μm. Scale bar = 50 μm.

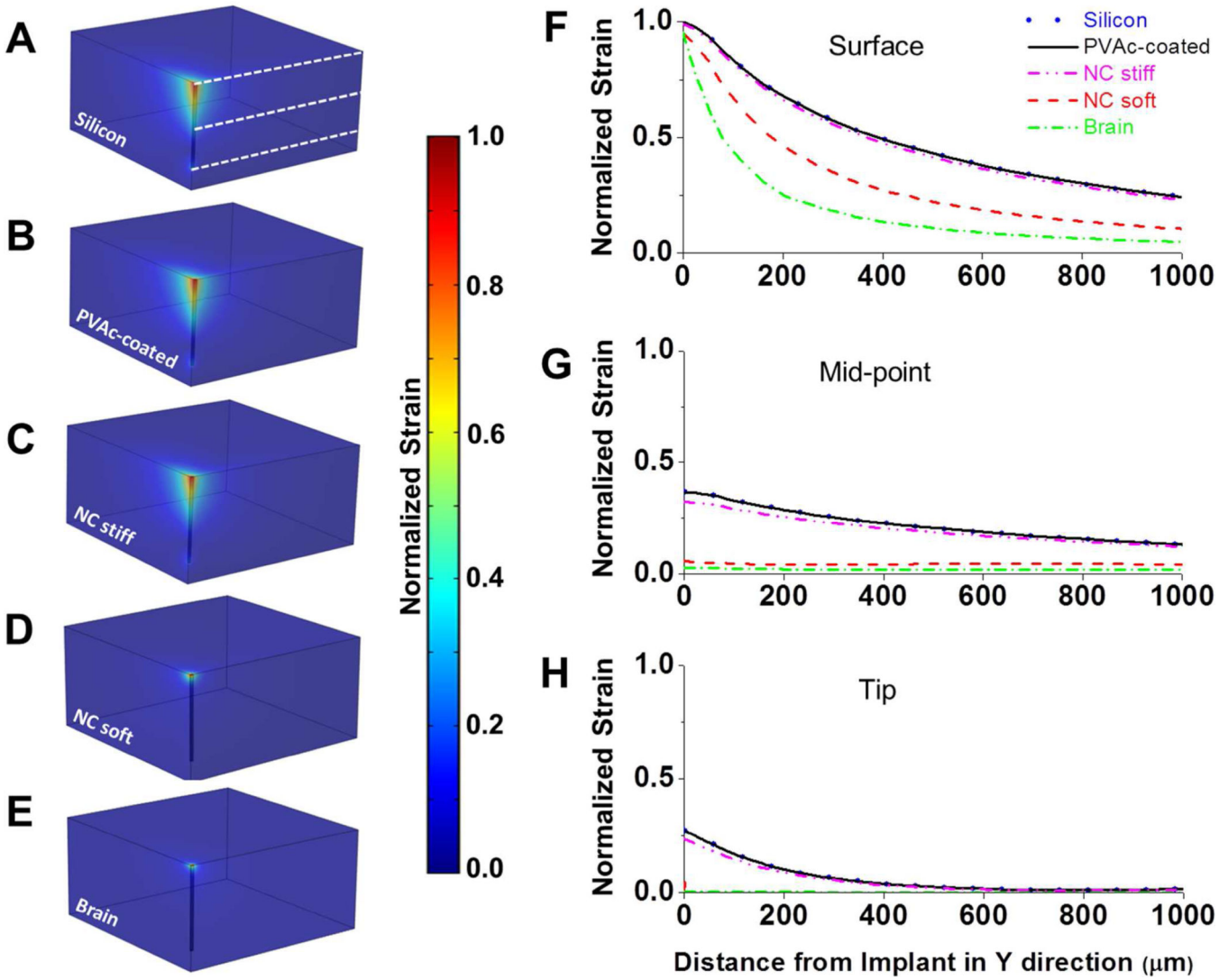

Figure 2.

(A–E) Predicted strain profiles induced by a tangential tethering force on (A) a bare silicon implant (*E*' = 200 GPa), (B) a silicon implant with a 15.5μm PVAc coating (*E*' = 78 GPa), (C) an implant created entirely of the PVAc nanocomposite material (63μm × 130μm) in the stiff state (*E*' = 5 GPa), (D) an implant created entirely of the PVAc nanocomposite material (63μm × 130μm) in the compliant soft state (*E*' = 12 MPa), and (E) a hypothetical implant that matches brain modulus (*E*' = 6 kPa). Strain profiles are normalized to the maximum induced strain surrounding the uncoated silicon probe. (F–H) Normalized strain profiles extending in the positive y-direction are taken from the brain surface, the implant's midpoint and implant's tip (levels are shown as white dashed lines in (A)). No significant differences were seen between the bare and coated silicon implants and stiff NC. Despite the nanocomposite implant having larger dimensions, the model demonstrated that the compliant nanocomposite implant would induce less strain on the surrounding tissue than both the uncoated and coated Si implants along their entire length. Additionally, no significant differences were seen between the compliant nanocomposite and a (hypothetical)

implant with a modulus that matches the one of the cortical tissue at the midpoint and tip levels.

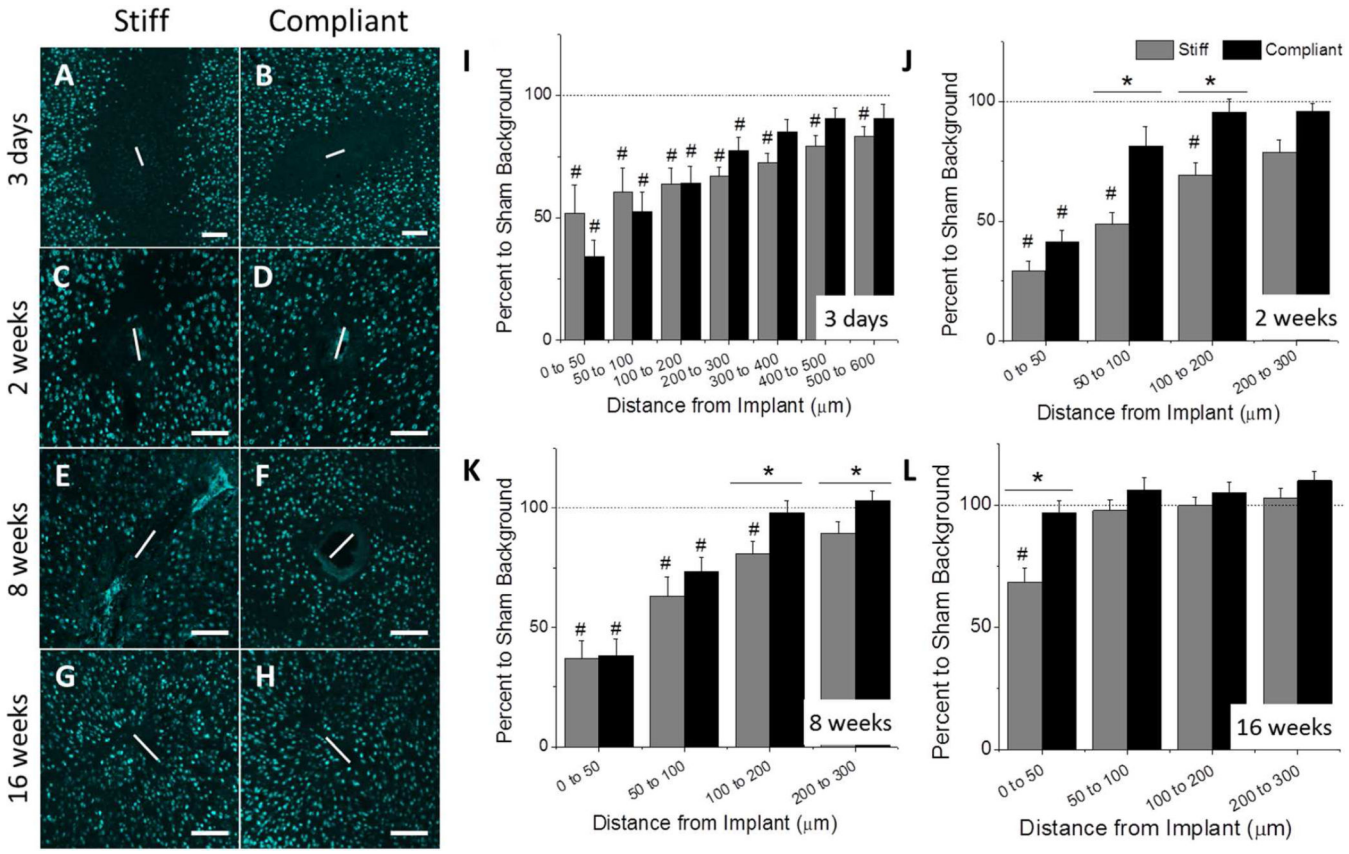

Figure 3.

Immunohistochemical analysis of neuronal nuclei (NeuN) around the implant site. Representative fluorescence microscopy images of stained tissue show that neuronal dieback around the stiff PVAc-coated silicon implant was significantly higher than in case of the compliant nanocomposite implant at various time points (3 days (A–B), 2 weeks (C–D), 8 weeks (E–F), 16 weeks (G–H)). The bar graphs show quantification of neuron densities. Statistical analysis identified several regions with significantly different neuron populations, which varied between time points. * Denotes significance between stiff and compliant samples; # Denotes significance between noted implant and age-matched sham control ($p < 0.05$). Scale bar = 100 μm. The horizontal dashed line represents the 100% neuron level as determined by quantification of age-matched sham animals. Error bars represent standard error.

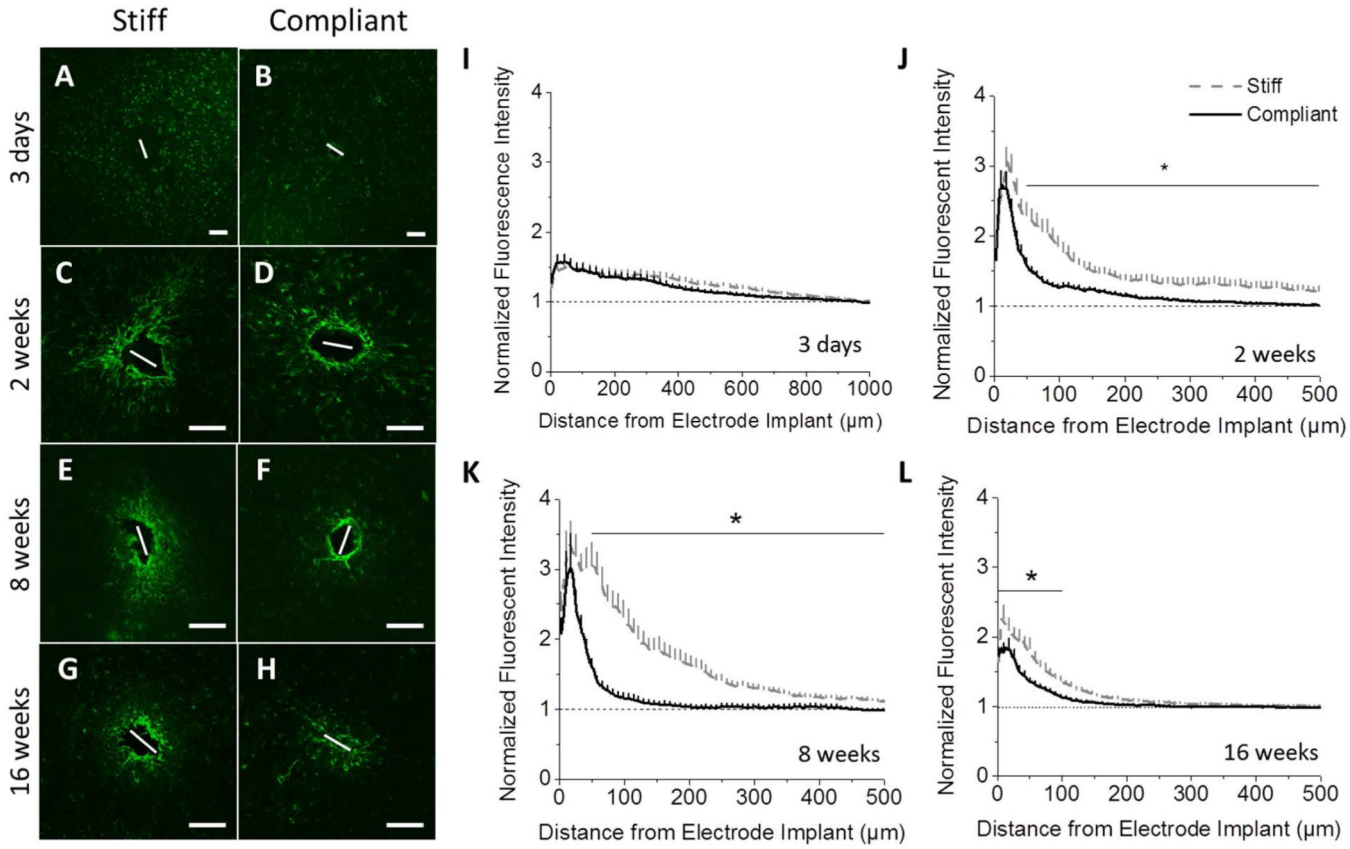

Figure 4.

Immunohistochemical analysis of the astrocytic scar. Representative fluorescence microscopy images of stained tissue show the formation of a more compact scar surrounding mechanically compliant implants (B, D, F, H), compared to the chemically-matched stiff implants (A, C, E, G) beginning at 2 weeks post-implantation. IHC staining for GFAP+ astrocytes after 2 weeks were seen at higher densities with broader distribution following implantation of the stiff implants compared to the mechanically compliant implants (I–L) ($p < 0.05$). Scale bar = 100 μm. Error bars represent standard error.

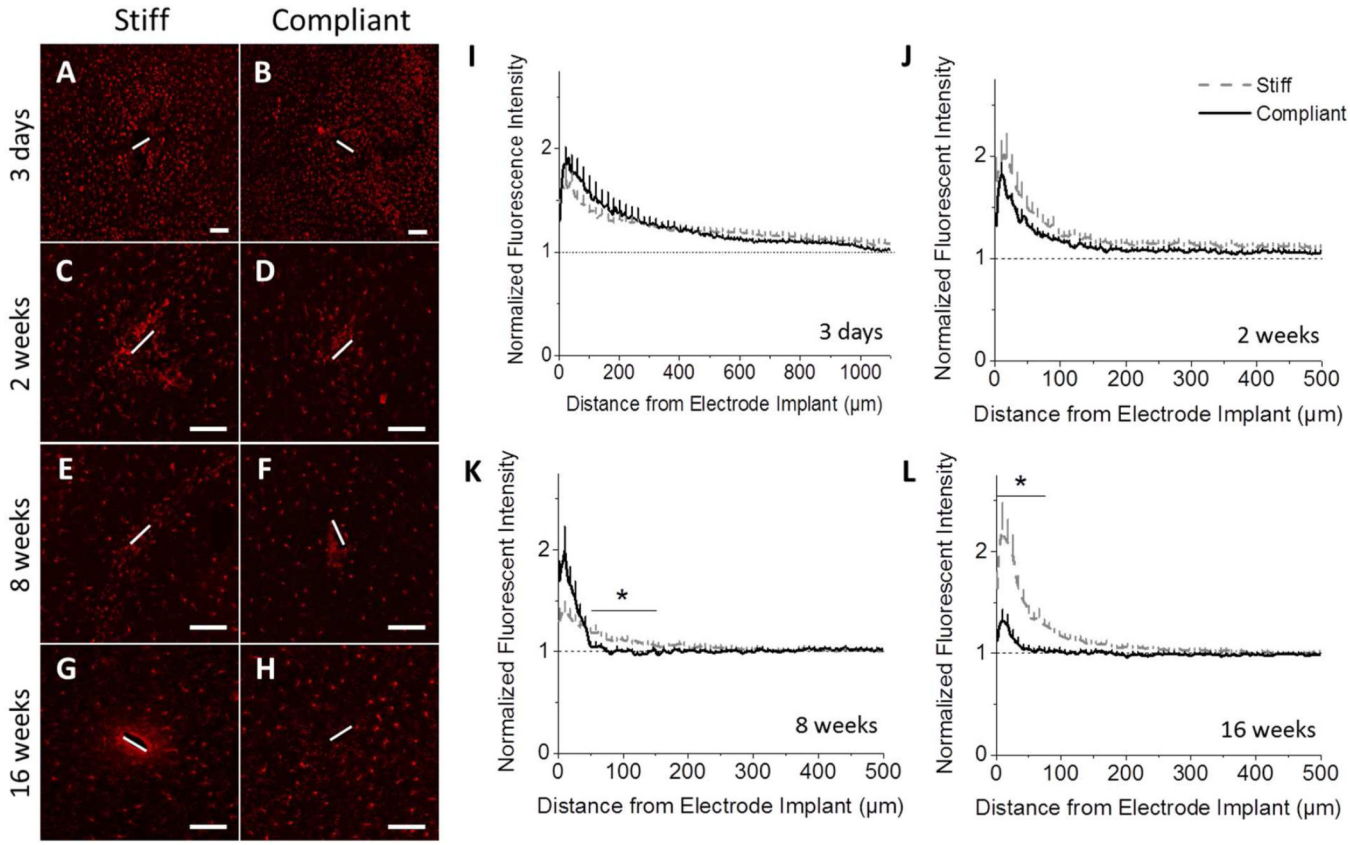

Figure 5.

Immunohistochemical analysis of total microglia/macrophages populations (Iba1). Representative fluorescence microscopy images of stained tissue show no effect of implant compliance at acute time points (3 days (A–B,I), 2 weeks (C–D,J)), but a significant increase in Iba1 immunoreactivity around stiff implants at chronic time points (8 weeks (E–F,K), 16 weeks (G–H,L)) ($p < 0.05$). Scale bar = 100 μm. Error bars represent standard error.

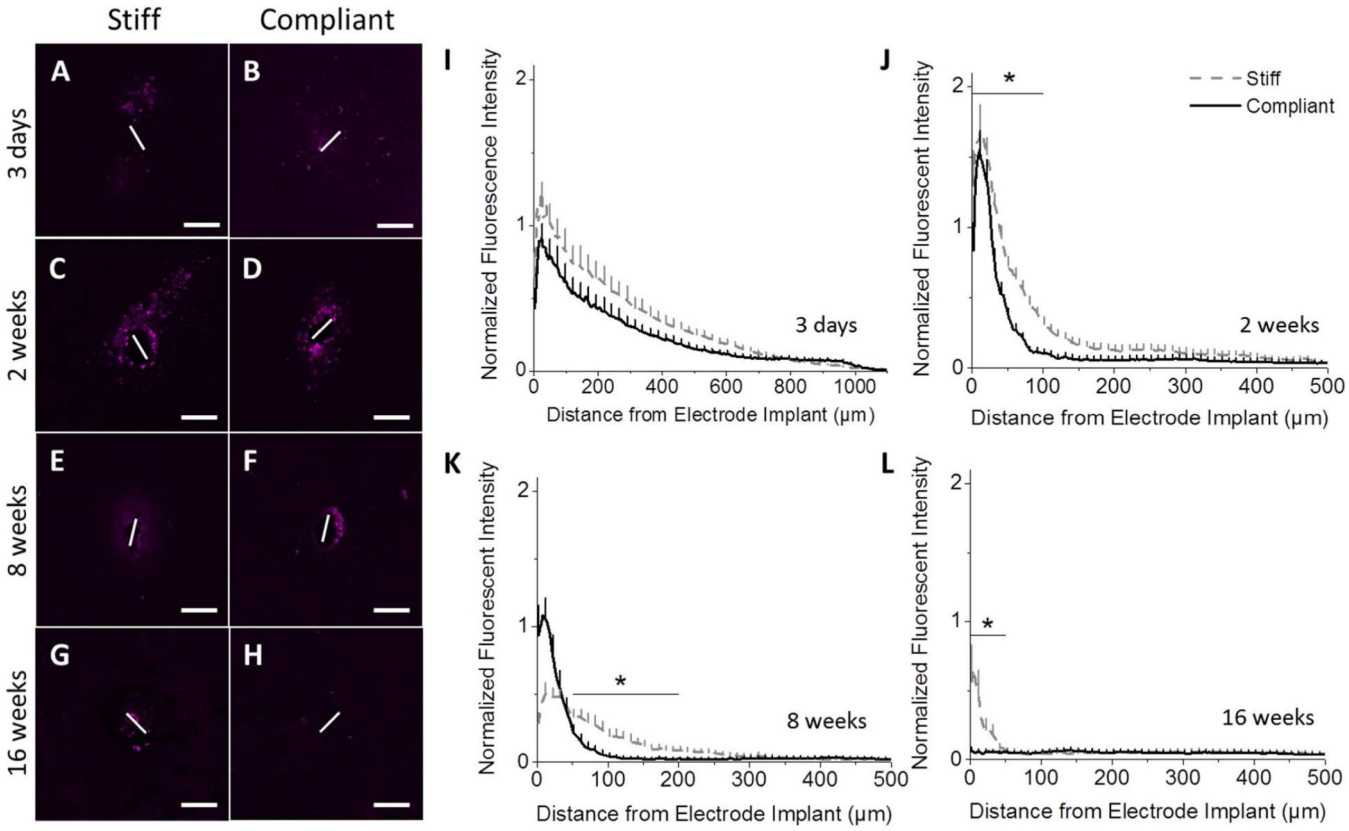

Figure 6.

Immunohistochemical analysis of CD68, a cellular marker for activated microglia/macrophages. Representative fluorescence microscopy images of stained tissue show a distinct benefit of mechanically compliant implants (B, D, F, H), compared to the chemically matched stiff implants (A, C, E, G). Starting at two weeks post implantation, IHC staining and fluorescent quantification showed increased expression of CD68+ tissue surrounding the stiff implants (I–L) ($p < 0.05$). Scale bar = 100 μm. Error bars represent standard error.

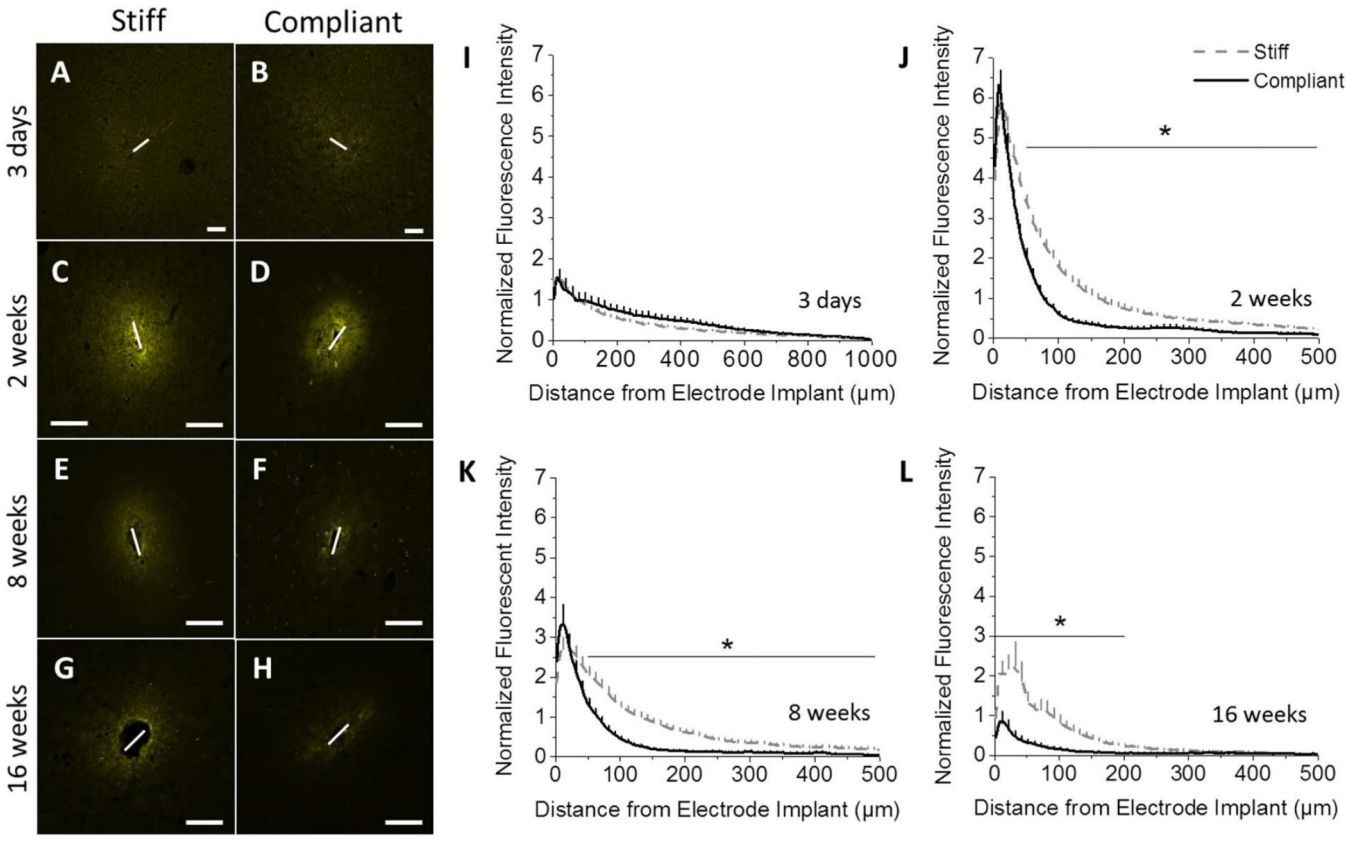

Figure 7.

Immunohistochemical analysis of IgG staining shows that the blood brain barrier integrity is improved for compliant implants, compared to stiff implants. Representative fluorescence microscopy images of IgG immunoreactivity show no difference three days post implantation (A, B). At all subsequent time points, a marked increase in IgG intensity was observed around the stiff implant (D, F, H) compared to the compliant implant (C, E, G). Quantification of the fluorescent intensity indicates significant differences between implants at 2, 8, and 16 weeks post implantation (J–L). ($p < 0.05$). Scale bar = 100 μm. Error bars represent standard error.

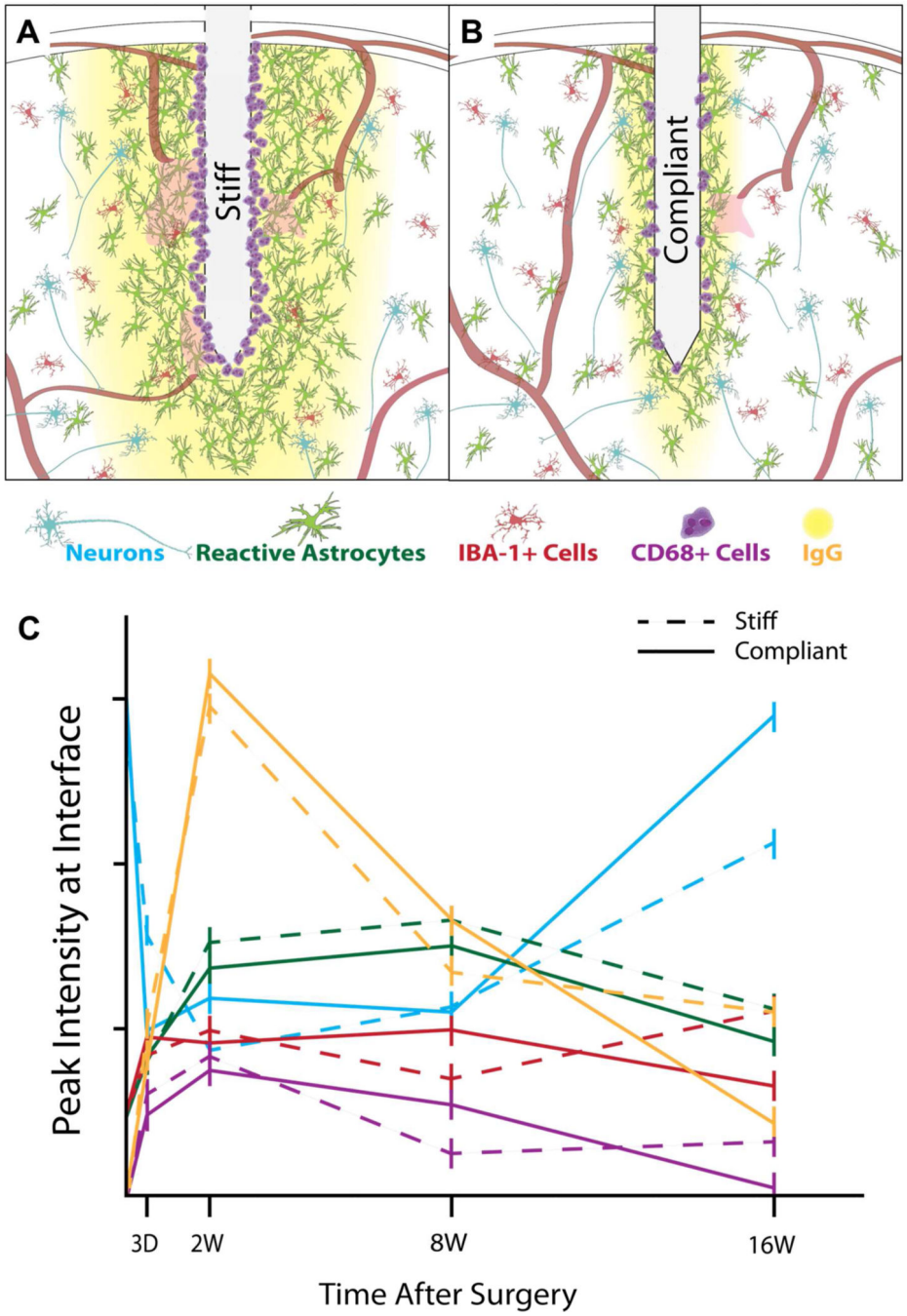

Figure 8.

Schematic representation of the tissue response around stiff (A) and compliant (B) implants. Stiff implants induce increased gliosis, BBB permeation, and neurodegeneration in comparison to compliant materials. (C) Graphical representation of the peak intensity of specific inflammatory markers over time, which shows a distinct advantage of compliant materials at chronic time points.